Chapter 3 Simulation studies

In chapter 2 three improved order tracking techniques have been developed theoretically. In this chapter, two simulation models will be used to investigate the effectiveness of the improved order tracking techniques. The first simulation model is a simple single-degree-of-freedom rotor model. The Vold-Kalman filter and computed order tracking (VKC-OT) and intrinsic mode function and Vold-Kalman filter order tracking (IVK-OT) will be validated in this model. The intrinsic cycle re-sampling (ICR) technique will be applied to a simplified gear mesh model to investigate its ability. In the following, three simulation studies are present in sequence. The focus in each of these simulation studies is described below:

1. The focus of the simulation studies using VKC-OT will be put on how the method features clear and focused order spectra compared with using each technique alone, so that the advantages of combing two traditional order tracking methods can be clarified.

2. The focus of the simulation studies using IVK-OT will be put on separation of vibrations that modulate orders in an IMF, especially for those speed non-synchronous vibrations so that IVK-OT demonstrates its ability which is intractable through other order tracking methods in isolation alone.

3. The focus of the simulation studies using ICR will be put on how the method interprets the ICR results and comparisons with traditional signal processing methods so as to demonstrate ICR as an alternative condition monitoring tool.

3.1 Single-degree-of-freedom rotor model simulation analysis

3.1.1 Single-degree-of-freedom rotor modelling

The first model treats the lateral response of a symmetric rotor as two uncoupled single-degree-of-freedom systems depicted in Figure 3.1. It is assumed that the rotor of mass M is mounted on bearings of total stiffness K and damping coefficient C, in both x- and y- directions. The rotor is assumed to rotate at an increasing speed. The time dependent external excitation forces *F(t)* are sinusoidal force combinations. In the first simulation, order terms 3 and 6 are included in the excitation forces. This means that force frequencies $3\times$RPM and $6\times$RPM are included in the model. The arbitrary system characteristics that are used for this investigation are listed in Table 3.1.

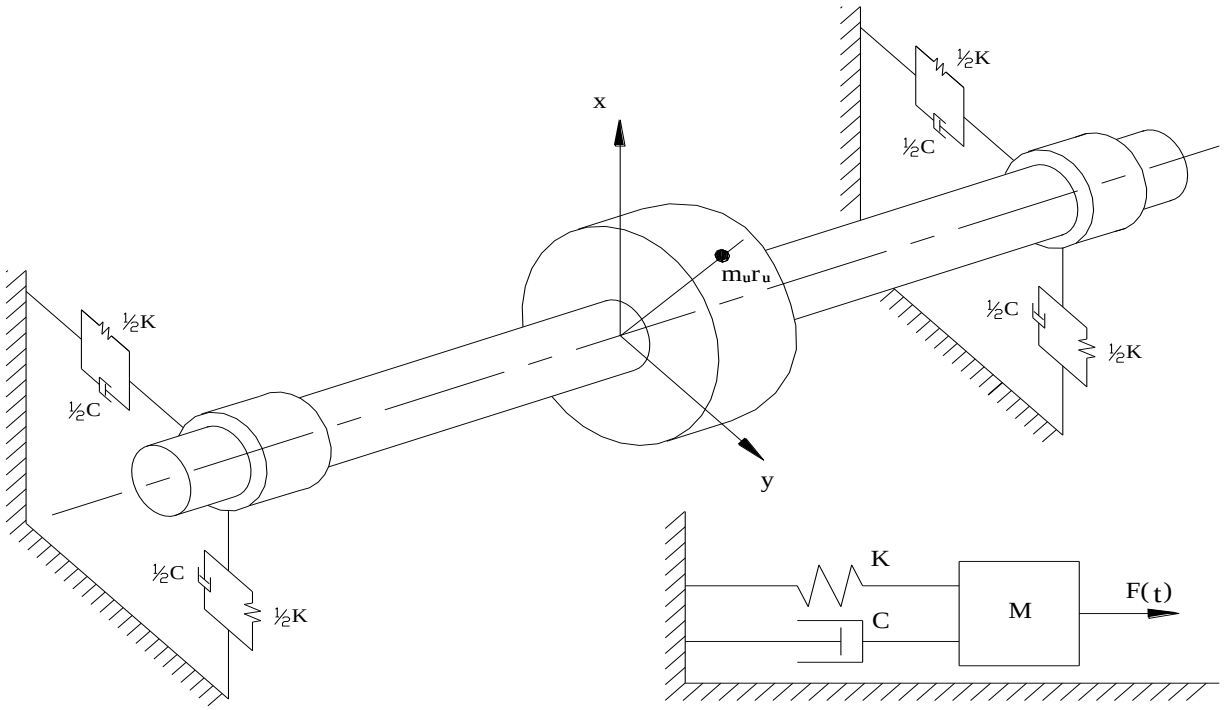

Figure 3.1 Simple symmetric rotor single-degree-of-freedom system

Table 3.1 System characteristics

Parameter	**Value**
Rotor mass M	20 kg
Damping coefficient C	100 Ns/m
Stiffness K	500 000 N/m
Eccentricity r_u	0.1 m
Unbalance mass m_u	0.05 kg
Initial time t_0	0 s
Final time t_f	5 s
Time steps	4096
Number of revolutions	100
Number of re-sampling intervals	100
Angular speed ω	$15.0796t^2$
Scenario 1	Excitation: $F = m_u\omega^2 r_u \sin(3\omega t) + m_u\omega^2 r_u \sin(6\omega t)$
Scenario 2	Excitation: $F = m_u\omega^2 r_u \sin(3\omega t) + m_u\omega^2 r_u \sin(6\omega t)$ Final System response = system response to F +Noise Noise: $100 \times randn(4096,1)$ (Normally distributed random noise with mean zero and standard deviation one).

It is simple to tune the different parameters of the system in the MATLAB environment. However some of the critical parameters must be commented on here. Mass and stiffness are two important parameters that determine the resonance frequency of the system and is proportional to the square root of K/M. Further, the excitation forces can be arbitrarily be generated in MATLAB. This is the one of the advantages of this simulation model, and makes it possible to include as many orders as desired, as well as simulate forces that might exist in real cases, for instance the fluctuation of load or beating external forces which will lead to the system response to be modulated. The familiar Runge-Kutta-Gill method was used to integrate the equations of motion for the simulated model to obtain system response.

3.1.2 Equations of motion for the single-degree-of-freedom system

In this rotor model simulation, the viscously damped case is considered and discussed in the following.

Assuming viscous damping the equation of motion is given by

$$M\ddot{X}(t)+C\dot{X}(t)+KX(t)=F(t) \tag{3.1}$$

where $X(t)$ is the system response in x- direction, and $F(t)$ is the simulated external excitation force function. The mathematical expression for the simulated force used in the VKC-OT method simulation study can be written as:

$$F(t)=m_u\omega^2 r_u \sin(3\omega t)+m_u\omega^2 r_u \sin(6\omega t) \tag{3.2}$$

This external force model is listed as scenario 1 in Table 3.1. For modelling of the external force exerted on the rotor, the force amplitude will be simulated as a normal force. This is not to say that all the force components will in reality be normal. But for simplicity, the mathematical expression for normal force is assumed to be:

$$F_{normal} = m_u \times \omega^2 \times r_u \tag{3.3}$$

where m_u is the mass unit, r_u is the distance from the centre to the mass unit and $\omega = \frac{d\theta}{dt}$ is the angular velocity of the rotor.

3.1.3 Single-degree-of-freedom system analysis

The system lateral acceleration response under the given external excitation force function in the time domain can be depicted as in Figure 3.2.

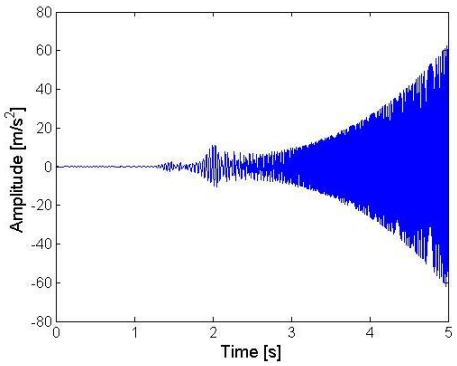

Figure 3.2 System response in the x direction

Based upon the choice of the system parameters and the external excitation force function (scenario 1), results of the system response can be anticipated. Due to the resonance, there must be a peak at 25.16 Hz in the corresponding spectrum. This can be determined from equation (3.4):

$$f = \frac{1}{2\pi}\sqrt{\frac{K}{M}} \tag{3.4}$$

At the same time, the 3rd and 6th orders due to the external forces should also appear in the response spectrum. However, due to the quadratic non-stationarity of the rotational speed, as is shown in Figure 3.3(a), this will definitely influence the appearance of the final spectral. In order to do the following computed order

tracking, the vertical lines in Figure 3.3(a) indicate the start time of each revolution. The RPM spectrum map is plotted to show frequency and amplitude variation of signals for this quadratic speed up case, as is shown in Figure 3.3(b).

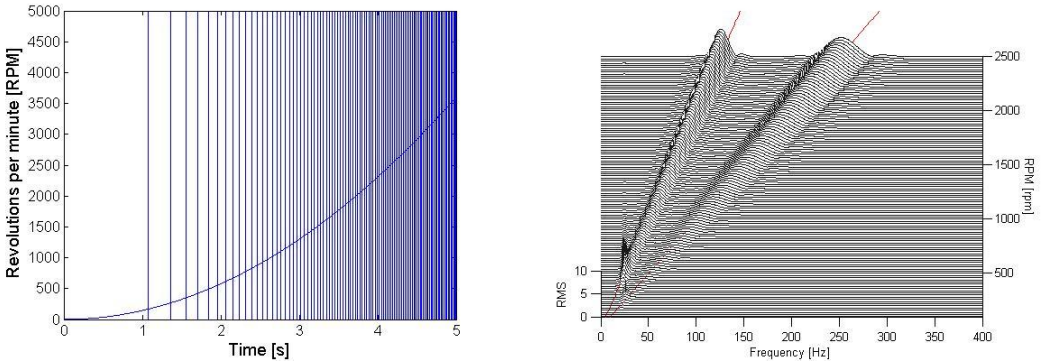

a) RPM b) RPM spectrum map

Figure 3.3 RPM and RPM spectrum map

Figure 3.3(b), shows a resonance at 25.16 Hz, which does not change with speed. Two dominant order related peaks, the 3rd and 6th orders, are marked with two lines. It can be seen that in between order peaks and resonance peak, there are some ripples which are caused by the quadratic rotational speed, although these are quite small. Based upon Figure 3.3(b) a clear picture of the system response with the progression of speed is presented.

3.1.3.1 Application of Vold-Kalman filter and computed order tracking

Once we obtain a clear picture of system response, the VKC-OT can be applied to the signals. And the purpose of this technique is to extract clear individual order components. Thus, let us examine the Power Spectral Density (PSD) results of the raw data, to confirm the observations of the above resonance and orders, and then focus on the 3rd order via VKF-OT, COT as well as VKC-OT. The PSD results of different techniques are then presented in Figure 3.4.

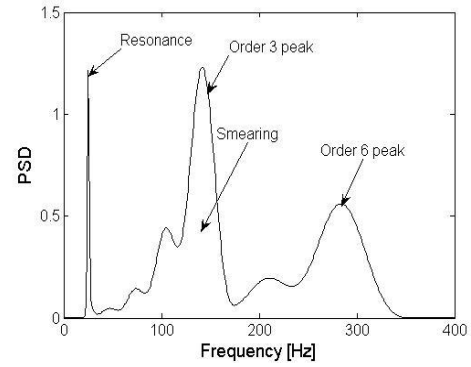

a. PSD on raw data

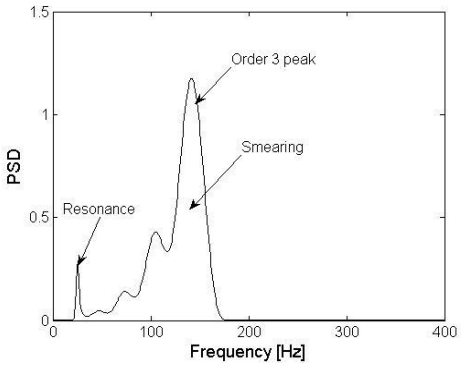

b. PSD on VKF-OT for 3rd order

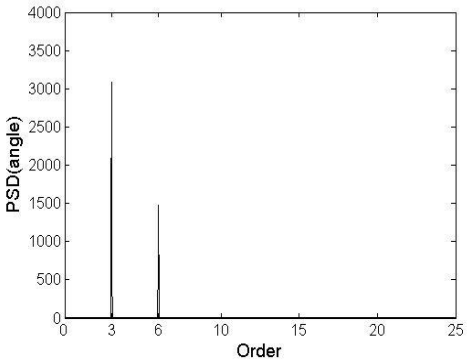

c. PSD on COT data

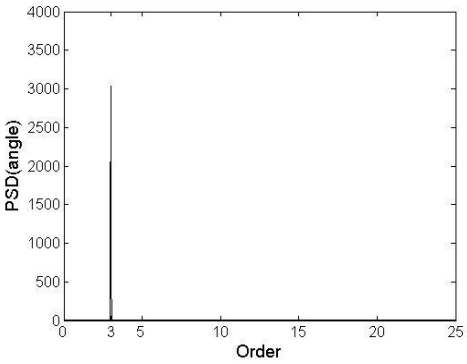

d. PSD on VKC-OT for 3rd order

Figure 3.4 PSD results raw data, VKF-OT for 3rd order, COT, VKC-OT for 3rd order

In Figure 3.4(a), which shows the PSD of the system response, there is one sharp resonance peak (fixed time-based frequency) and two rounded order peaks (smearing due to the non-stationarity of the time-based data caused by the increasing excitation frequencies). Figure 3.4(b) is the result of performing a PSD on VKF-OT which highlights the 3rd order information and removes the 6th order. The non-stationary smearing effect is still visible in the spectrum. The system resonance is also largely removed. Remnants of the resonance remain because of the 50% relative filter bandwidth which was used. (The 50% relative filter bandwidth means that the ratio of the instantaneous absolute filter bandwidth

to the instantaneous rotational speed frequency is 0.5. Here it is necessary to elaborate on the choice of pass band filter for Vold-Kalman filter tracking. One must be very cautious that for the narrower filter bandwidth, better tracking abilities do not necessarily hold. The Vold-Kalman filter obeys a time frequency relationship, $B_{3dB} \times \tau = 0.2$, where B_{3dB} is the $3dB$ bandwidth of the Vold-Kalman filter and τ is the time it takes for the time response to decay by $8.96\,dB$ (Herlufsen, 1999). It should be noticed that the relationship between B_{3dB} and τ is inversely proportional. Therefore, a narrower filter pass band will result in a longer time response to track the changes of signals. As a result, the narrow pass band reduces the permissible rate of change in rotational speed. The choice of filter bandwidth needs to be done very carefully. For an example analysis, the reader may refer to Wang and Heyns (2009) and for details on the choice of the filter bandwidth the reader may refer to Herlufsen (1999).

Figure 3.4(c) displays the result of COT that there are two clear peaks in the order spectrum at the 3rd and 6th orders respectively. This is because of the data being generated for an ideal linear system with sinusoidal external excitation, and the re-sampling process of COT which rearranges the data to become stationary. The data therefore represent stationary harmonic waves which are ideal for Fourier analysis.

It should be noted that the numerical values of the PSDs in Figures 3.4(a and b) and 3.4 (c) differ significantly. It should also be emphasized that the number of samples calculated by COT is different from traditional Fourier analysis. Since the given rotor rotates 100 revolutions within 5s and each revolution is evenly sampled with 100 angular intervals, therefore the resultant samples for COT analysis become 10000 instead of 4096. Besides, in Figures 3.4(a and b) the PSD describes how the energy associated with the time domain series is distributed with

frequency. The unit is $(m/s^2)^2/Hz$. Figure 3.4(c) however describes how the energy of an angular domain series is distributed with order. Fundamentally the energy associated a particular order is distributed over a wide range of frequencies on the time domain based PSD, due to the non-stationary nature of the rotational speed. However on an angle domain based PSD the energy associated with a specific order is reflected at only one order value. The unit is $(m/s^2)^2/order$. It is actually a sum of distributed energies in the frequency domain for a specific order. Thus, in order not to confuse readers, the units of the PSDs are not indicated in the above figures at this time. However, the acronym 'PSD' is used on figures representing time domain based Power Spectra Density, while angle domain based PSD figures are indicated by 'PSD (angle)'.

It can be seen that Figure 3.4(c) present clear peaks. However it should still be borne in mind that the re-sampling process of the angle domain based method changes the number of samples of the raw data. In this case, it is performed under the assumption of zero rotational acceleration within each revolution and thus it re-samples signals in each revolution with equal intervals. Notice that the number of samples per revolution is a parameter that may be chosen arbitrarily by the analyst. These choices may render different numbers of re-sampled samples as well as variation of the value of re-sampled amplitude and as such also influence the final result in numerical values. This has been discussed in Chapter 1 paragraph 1.3.1. Therefore, once the number of samples has been chosen it should be kept consistent in all applications of the technique. Most importantly however, angle domain based PSD (angle) cleans up the smearing spectrum from frequency domain into the order domain and features distinct clear amplitude orders.

Besides, it should also be observed that the system resonance can hardly be recognized in Figure 3.4(c). This is because the re-sampling occurs in the angle

domain, which means the sampling interval changes to constant angle rather than constant time interval, and the Fourier analysis actually only captures periodic signals with respect to angle instead of time (as is the case for resonance). Thus COT deemphasizes the system resonance after the re-sampling.

If the VKC-OT procedure suggested in chapter 2 is however applied, Figure 3.4(d) is obtained. It is the application of COT on the filtered 3rd order by VKF-OT. This figure shows a single clear 3rd order peak in the spectrum, and illustrates the advantage of the combined use VKF-OT and COT to obtain diagnostic information about a system. Although both Figures 3.4(c) and (d) clearly indicate the system information, Figure 3.4(d) separates the individual 3rd order from the raw data, which makes it possible to further investigate the 3rd order information itself and therefore has an advantage compared to Figure 3.4(c).

In the above simulation, the response data are generated from an ideal linear system with ideal sinusoidal external excitation, which simplifies the interpretation of the spectra. But, if external noise is added to the system response, the resultant observed response data = response to the external force + noise. To illustrate this, the simulation model uses scenario 2 (in Table 3.1) and the corresponding PSD results for different techniques are now shown in Figure 3.5.

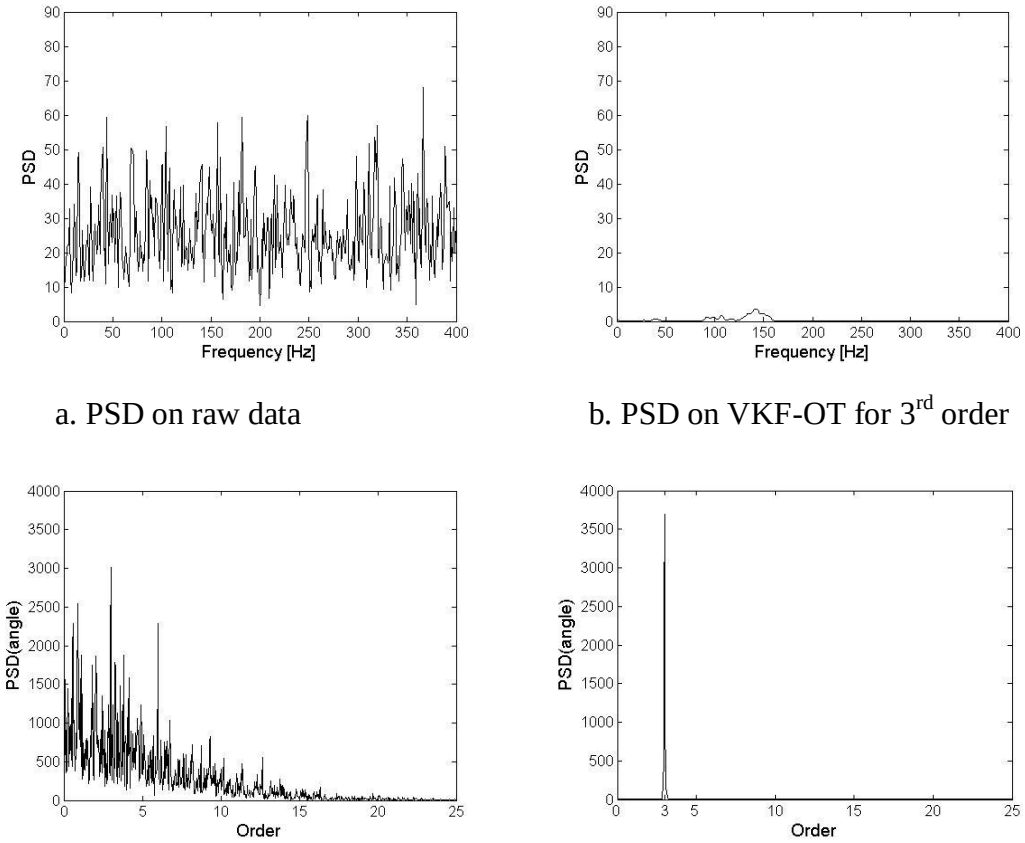

a. PSD on raw data

b. PSD on VKF-OT for 3rd order

c. PSD on COT data

d. PSD on VKC-OT for 3rd order

Figure 3.5 PSD results for scenario 2 (with noise)

Little can be learnt from the spectrum in Figure 3.5(a) because the noise overwhelms the signal. Figures 3.5(b) and (c) are the PSD and PSD (angle) after VKF-OT and COT respectively, and do provide some insight into the system, albeit limited compared to Figure 3.4. It should also be noticed that the energy in Figure 3.5(b) is much lower than Figure 3.5(a). This indicates that the VKF-OT technique largely excludes the influence of noise and focus on the order of interest. Finally however Figure 3.5(d) provides another clear 3rd order peak largely excluding the influence of noise and non-stationarity. This result further demonstrates that combined use of VKF-OT and COT can significantly enhance

the result from Fourier analysis. And the VKC-OT technique does provide an excellent ability to extract clear individual order component.

3.1.3.2 Application of intrinsic mode function and Vold-Kalman filter order tracking

To investigate the ability of the IVK-OT technique, the above simulation model will be used again, however a more complex signal composition is now simulated. Since the main advantage of this technique lies in further decomposition of the IMFs and through the process, order signals and vibrations that modulate orders in IMFs can be separated. Vibrations that modulate orders are often key signatures of machine faults. However they might be quite unpredictable and may be speed synchronous or non-synchronous. Thus a more comprehensive signal should be generated to validate the distinct abilities of the IVK-OT method. Therefore, the characteristics of the model are changed and shown Table 3.2.

Table 3.2 Simulation model characteristics of the SDOF rotor

Parameter	**Value**
Rotor mass M	20 kg
Damping coefficient C	100 Ns/m
Stiffness K	500 000 N/m
Eccentricity r_u	0.1 m
Unbalance mass m_u	0.05 kg
Initial time t_0	0 s
Final time t_f	5 s
Time steps	4096
Number of revolutions	100
Number of re-sampling intervals	100

Angular speed ω_1	$\omega_1 = 15.0796\ t^2$ rad/s
Angular speed ω_2	$\omega_2 = \dfrac{\omega_1}{2.5} = 6.0318\ t^2$ rad/s
External excitation	$F = A_{m1}\sin(3\omega_1 t) + 0.5A_{m1}\sin((3\times 0.9)\omega_1 t) + A_{m2}\sin(3\omega_2 t)$ N 1) Speed synchronous amplitude $A_{m1} = m_u\omega_1{}^2 r_u \quad A_{m2} = 2m_u\omega_2{}^2 r_u$ 2) Speed non-synchronous amplitude $A_{m1} = m_u\omega_1(1-\sin(2\pi f_m t)^2 r_u$ $A_{m2} = 2m_u\omega_2(1-\sin(2\pi f_m t)^2 r_u$ $f_m = 5Hz$
Observed signals	$y = y_F + A\sin(2\pi ft) + noise$ 1) y_F is the response due to the external excitation 2) $A\sin(2\pi ft)$ is a constant sinusoidal component at $f = 100Hz,\ A = 7.5\%rms(y_F)$ 3) Random noise is set to be $noise = 5\%rms(y_F)$ in amplitude.

To clarify the composition of observed signals, the signal composition is categorized as speed synchronous and non-synchronous vibrations which are depicted in Figure 3.6.

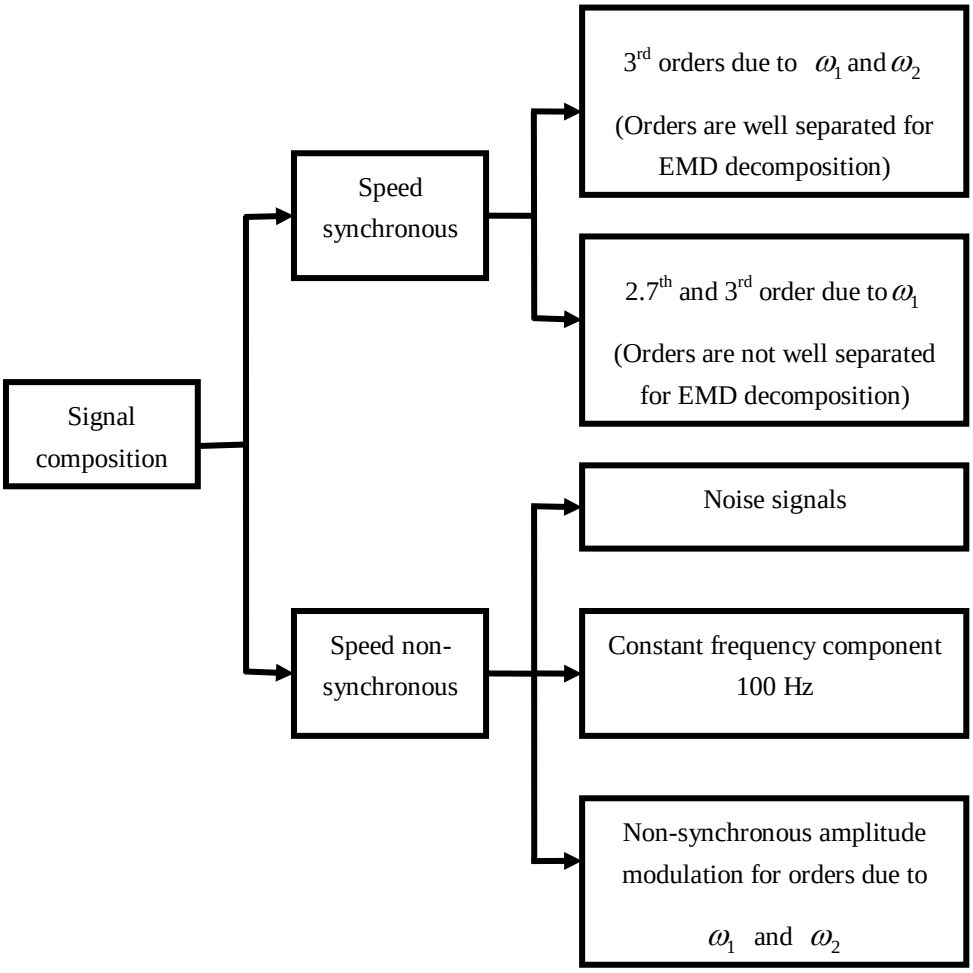

Figure 3.6 Signal composition of simulation study

Firstly, based upon Feldman's separation criterion shown in Figure 2.2 in chapter 2, two cases are considered with the speed synchronous or order signals. The 3rd orders due to rotational speed components ω_1 and ω_2 are well separated for EMD decomposition. The 2.7th and 3rd orders of ω_1 are not suitable for decomposition by EMD. The amplitude and frequency relationships for these cases are also indicated in Figure 2.2.

Among the speed non-synchronous signals, random noise is included since it is inevitable in reality, and a constant signal at 100 Hz is also added to simulate a

typical multiple of electrical line frequency. For comparative purposes, speed synchronous amplitude and speed non-synchronous amplitude modulation for external excitation force are both simulated for comparison. The details are listed in Table 3.2. The Runge-Kutta-Gill method was again used to obtain the system response in a MATLAB environment.

a. Overall signal analysis

Considering the response in the vertical x- direction, the calculated acceleration time response, the corresponding frequency spectrum and the RPM spectrum map are plotted in Figure 3.7 for displaying the nature of the signals by traditional signal processing methods. Where not specifically mentioned, all the figures are obtained for the speed non-synchronous amplitude modulation case.

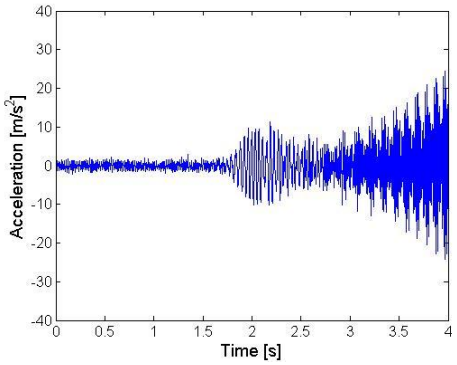

a. Time response

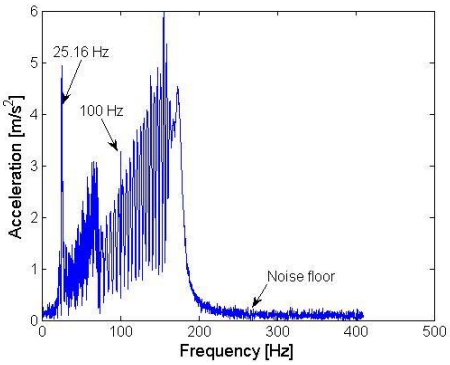

b. Frequency spectrum

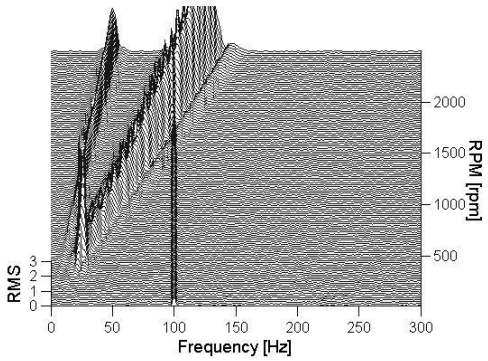

c. RPM spectrum map (based upon rotational speed ω_1)

Figure 3.7 Signal processing of raw signals

Figure 3.7(a) is the time response of the system. A clear beating effect of the signals can be seen which is due to the closely spaced sinusoidal external excitations. Figure 3.7(b) shows the signal in the frequency domain where a system resonance is present at $f_n = \frac{1}{2\pi}\sqrt{K/M} = 25.16$ Hz. The system resonance is due to the choice of the system parameters M and K. This characteristic of the system is independent of the external forces. The smeared hump with the oscillating ripples is due to the quadratically increasing rotational speed, and the two sets of external forces that cause the high oscillating ripples over a wide range. The random noise floor is also seen in the spectrum. Further, the RPM spectrum map in Figure 3.7(c) shows how the signal evolves with speed. Two sets of speed varying signals can be observed and a clear 100 Hz component appears throughout the speed range and it is not influenced by speed. The traditional signal processing methods provide a clear understanding of the signal.

b. Application of EMD

EMD may now be used to decompose the signals into IMFs, using the Hilbert Huang Transform Data Processing System (HHT-DPS1.4) obtained from NASA Goddard Space Flight Centre. The decomposition results are shown in Figure 3.8

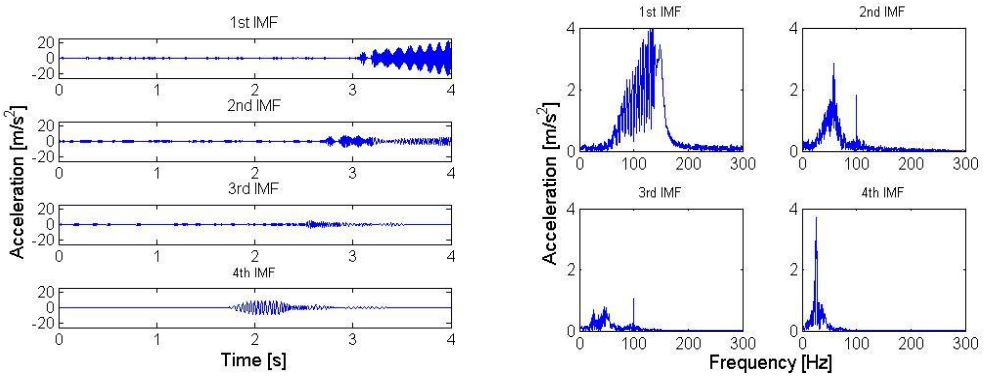

a. IMFs b. Frequency spectrum of IMFs

Figure 3.8 IMFs from EMD

Figure 3.8(a) indicates that the 1st IMF also exhibit beating effects similar to that seen in Figure 3.7(a). Figure 3.8(b) shows the frequency spectra of these IMFs. The 1st IMF spectrum shows a smeared hump with the oscillating ripples which indicate that it captures the system responses due to the closely spaced external forces. It is also clear that the system resonance is not included in the 1st IMF. The 2nd IMF also shows oscillating ripples in the spectrum in a lower frequency range, as well as a clear 100 Hz component. Clearly the oscillating ripples in Figure 3.7(b) are being separated into different IMFs and the system resonance is not evident in both 1st and 2nd IMFs. The 3rd IMF again shows part of the oscillating ripples in the spectrum and also a 100 Hz component, albeit much smaller than those in the 2nd IMF. Lastly, the 4th IMF clearly shows system resonance and it does suggest that the system resonance is being separated and specifically concentrated in the 4th IMF. From these observations of the EMD results, it is found that the system resonance components, 100 Hz component as well as the oscillating ripples are separated into different IMFs. However the physical significance of the ripples in the different IMFs is still vague.

c. Using computed order tracking to recognize order components in IMF

Therefore order tracking techniques are now used to assist in the further clarification and decomposition of the signals. Computed order tracking (COT) is applied to the IMFs referring to ω_1 in Figure 3.9. In this signal analysis, the observed signal from the speed synchronous amplitude case is also plotted for comparison. The two computed order tracking results are shown in Figure 3.9 (a) and (b). In order to compare order components in different IMFs, the highest order amplitude in the 1st IMF is used to normalize all four order spectra maps so that the amplitude relationship between IMFs can be easily seen. (This normalized process is applied to all the following order domain analyses).

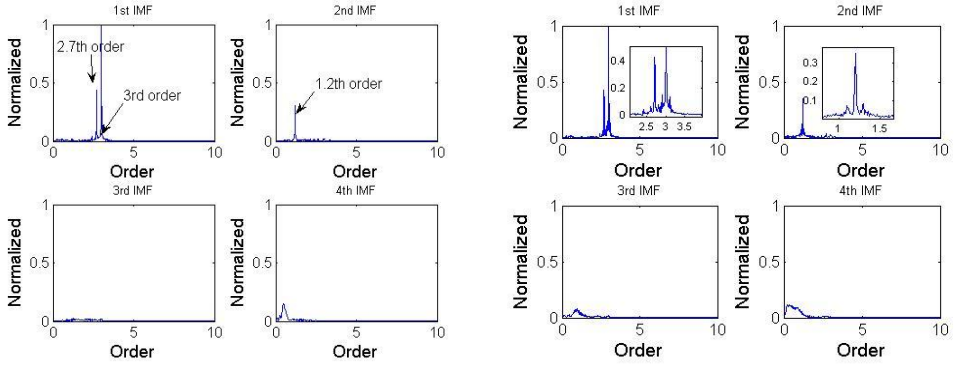

a. Speed synchronous amplitude b. Speed non-synchronous amplitude

Figure 3.9 Normalized order spectra for IMFs

Looking at Figure 3.9 (a) of the speed synchronous amplitude case, it is seen that the 1st IMF clearly consists of the 2.7th and 3rd orders. The 2.7th order is nearly half of 3rd order in amplitude, which corresponds well to the preset amplitude ratio of 0.5 in the force components. In the 2nd IMF a 1.2th order component can be seen. The 2nd IMF indeed captures another rotating speed signal, since it corresponds very well to the speed ratio of 2.5 between the two speeds. However, compared with dominant 1st IMF, this 1.2th order is much smaller. Besides, it should still be remembered that in Figure 3.8(b), both 3rd and 4th IMFs show clear spectra in the frequency domain, especially for the 4th IMF of its system resonance component. However since the re-sampling process of COT transforms equal time intervals to equal angular intervals, and then the Fourier analysis actually captures only the periodic signals with respect to angle instead of time (as is especially for the case of resonance), the system resonance and signals that non-synchronous with rotational speed, therefore, are de-emphasized once the re-sampling has been performed. This also appears in the previous VKC-OT application. As a result, the 3rd and 4th IMFs in the order spectra become much smaller than they are in frequency domain. This indicates that both 3rd and 4th IMFs are not closely related to rotational speed. Through COT analysis of IMFs

in Figure 3.9 (a), it may be concluded that the system responses due to the excitation at the two rotating speeds are well separated by EMD into the 1st and 2nd IMFs, however the close varying harmonics are not being separated in the 1st IMF.

Then, the speed non-synchronous amplitude modulation case is studied in Figure 3.9(b). Firstly, compared to Figure 3.9(a), four similar resultant order maps are rendered. Again, EMD successfully separates the system responses due to the two rotating speeds into the 1st and 2nd IMFs. At the same time it can not further separate close varying harmonics in 1st IMF. However upon closer inspection of the zoomed figures of the 1st and 2nd IMFs, sidebands appear in the order spectrum which do not occur in the speed synchronous amplitude case in Figure 3.9(a). This is due to the non-synchronous amplitude modulation of external excitation force. These signals are very important indications of system changes. However, they are quite small and easy to be neglected. In order to clearly visualize them, the zoomed figures are also plotted on top of the figures in Figure 3.9(b). Besides, with regard to these sidebands the traditional VKF-OT method can not perform the filtering properly since the sidebands are not synchronous with speed. Thus, it suggests further decomposition. The 1st IMF is chosen for illustrating this further decomposition process.

d. Application of Vold-Kalman filtering on IMF

The Vold-Kalman filter can thereafter be used for the 1st IMF in the speed non-synchronous amplitude modulation case. Firstly, the dominant 3rd order is extracted. A 20% relative filter bandwidth is used. In the top figure of Figure 3.10(a), the spectra of the 1st IMF and 3rd order are superimposed together and therefore the relationship between them can be seen. The corresponding time waveform of 3rd order is also plotted in the right hand side top figure of Figure 3.10(b). After the extraction of the 3rd order, the rest of signal is also plotted in the frequency domain in the bottom figure of Figure 3.10(a). The 2.7th order is

also extracted and its corresponding time wave is plotted in Figure 3.10(b). Clearly the majority of signals are being extracted since 1st IMF is a strongly speed related IMF.

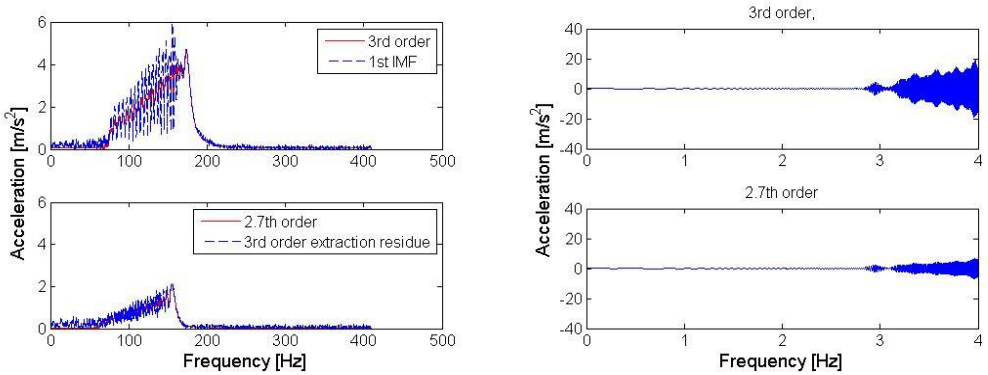

a. Spectrum maps b. Time waveform

Figure 3.10 Separation of 2.7th and 3rd orders

With the help of computed order tracking to recognize orders and Vold-Kalman filter order tracking to extract them in time waveforms, the 2.7th and 3rd order signals that are synchronous with the rotational speed are successfully decomposed from the 1st IMF. However, vibration signals that are non-synchronous with the rotational speed, especially for this case with amplitude modulation, should be further attended to. At this stage, if only VKF-OT was to be applied to the raw signals so that all the recognized orders are extracted through VKF-OT, the sidebands of the orders would be rendered and mixed together. However, instead of mixing this information, the combined IMF and VKF-OT provides the ability of focusing on the sidebands associated with the orders of interest and distinguish them for analysis. This is a unique capability of the sequential use of EMD and order tracking methods. The results are plotted in Figure 3.11.

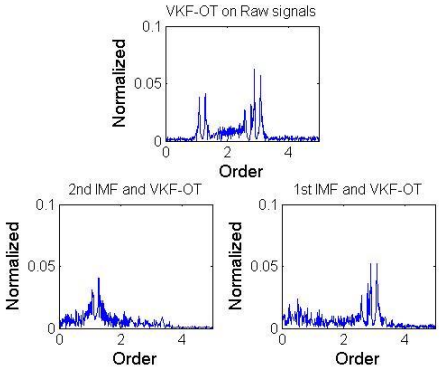

Figure 3.11 Separation of 1.2th and 3rd order sidebands

The top plot in Figure 3.11 is the order domain results of raw signals after subtracting the 1.2th, 2.7th and 3rd orders by VKF-OT. It can be seen that two sets of sidebands of 1.2th and 3rd orders remain. Since the VKF-OT can not further extract non-synchronous amplitude modulation sidebands properly, the traditional order tracking method stops here. However by using 1st and 2nd IMFs and VKF-OT, all recognized orders can be filtered out and render separated sidebands in the bottom two figures of Figure 3.11. (Note that the 100 Hz component in the 2nd IMF can also be extracted by VKF-OT through considering it as a constant rotational speed at $RPM = 100 \times 60 = 6000(rpm)$). The bottom two figures achieve further separation of sidebands with the help of different IMFs. As a result, 1.2th and 3rd order sidebands are well separated into two figures which are intractable by traditional VKF-OT as is shown in the top figure of Figure 3.11. If further comparing the results of sequence use of two methods to EMD as well as VKF-OT alone around 3rd order, it leads to Figure 3.12.

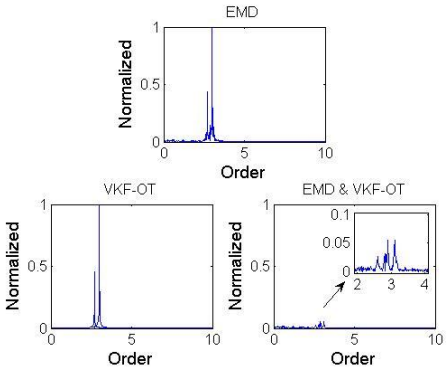

Figure 3.12 Results comparison of EMD, VKF-OT and sequence use of EMD & VKF-OT (use 1st IMF to illustrate)

For the EMD result at the top of Figure 3.12, the 1st IMF captures both 2.7th and 3rd order as well as some sidebands around dominant orders. Clearly the amplitude modulation effects on sidebands are fairly small and are emaciated by the dominant orders. EMD can not further decompose this 1st IMF. Through VKF-OT, the 2.7th and 3rd orders are properly extracted and superimposed together in the figure. However, no sideband information appears in the spectrum and therefore the ability of detecting the changes on amplitude modulation effects is lost. More importantly, since the amplitude modulation is non-synchronous with rotational speed, it is not amenable to VKF-OT. Through the sequential use of EMD and order tracking methods, the sideband information is however separated in the last figure of Figure 3.12. From Figure 3.12, it is clear that the amplitude modulation sidebands could not be extracted by using EMD or VKF-OT alone.

In the context of machine diagnostics, it should be emphasised that the un-extractable amplitude modulation effects by using either EMD or VKF-OT, are extracted through combining the two techniques in sequence. The extraction of amplitude modulation effects around the 3rd order excludes the interference from the other order, i.e. 1.2th order, so that analyst may focus on the amplitude variations of the 3rd order. This makes the condition monitoring process more flexible and selective. In short, the sequential use of EMD and order tracking

methods provides an advantage compared to EMD or VKF-OT in isolation. Information which would be un-extractable through both techniques alone can be achieved by combining them in sequence.

3.2 Simplified gear mesh model simulation analysis

3.2.1 Simplified gear mesh modelling

A simplified gear mesh model shown in Figure 3.13 is used for the simulation study. This model was also used by Stander and Heyns (2006) to investigate the advantages of instantaneous angular speed for gearbox condition monitoring. It is adopted here to obtain simulated gear mesh signals. The model comprises four degrees of freedom. A unique feature of the model is the incorporation of a translating mass M_1 to represent conventional translational vibration monitoring on the gear case. Model characteristics are given in Table 3.3.

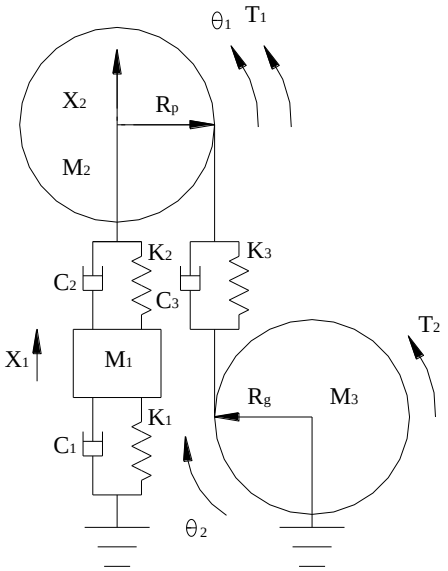

Figure 3.13 Dynamic gear mesh model

Table 3.3 Model characteristics and system load

M_1	Translating mass	0.05 kg
M_2	Pinion mass	0.05 kg
M_3	Gear wheel mass	0.05 kg
I_1	Inertia of pinion gear $I_1 = \frac{1}{2} M_2 R_p^2$	2.5×10^{-6} kg • m^2
I_2	Inertia of gear wheel $I_1 = \frac{1}{2} M_3 R_g^2$	2.5×10^{-6} kg • m^2
K_1	Structural damping	100 kN/m
K_2	Bearing stiffness	100 kN/m
K_3	Gear mesh stiffness	$100\{1 - 0.01\sin(N \times \theta_1)\}$ kN/m
C_1	Structural damping	1.2 Ns/m
C_2	Bearing damping	1.2 Ns/m
C_3	Gear mesh damping	1.2 Ns/m
R_p	Pinion base circle radius	0.01 m
R_g	Gearwheel base circle radius	0.01 m
N	Number of gear teeth	10
GR	Gear ratio	1:1
f_s	Sampling frequency	8192 Hz
I	Number of re-sampling intervals within one revolution	2000

Input torque	$T_1 = 1 + 0.1\sin\omega t$, $\omega = 2\pi \times 25$
Load	$T_2 = K_s\dot{\theta}_2^{\,2}$, $K_s = 16.2$

The gear mesh stiffness K_3 is modelled to allow a 2% sinusoidal variation of the nominal gear mesh stiffness so as to simulate the fundamental gear mesh harmonic. This is based upon the work of Howard et al. (2001). A simple viscous damping model is assumed.

A unity input torque T_1 is applied to the input pinion of the model with a 20% variation in time in order to simulate the fluctuating input and therefore causes the variations of rotational speed. The load on the system is set proportional to the square of the gearwheel speed, which enables the system to accelerate up to a nominal speed during the simulation. A proportional constant K_s is chosen to control the resultant nominal steady-state rotational speed of the system. Choosing K_s = 16.2, one obtains a nominal system rotational speed of 1500 rpm.

The equations of motion describing the model are presented in Eqs. (3.5) – (3.8)

$$M_1\ddot{X}_1 + (C_1 + C_2)\dot{X}_1 + (K_1 + K_2)X_1 - C_2\dot{X}_2 - K_2X_2 = 0 \tag{3.5}$$

$$M_2\ddot{X}_2 + (C_2 + C_3)\dot{X}_2 + (K_2 + K_3)X_2 - C_2\dot{X}_1 - K_2X_1 - C_3R_g\dot{\theta}_2 \tag{3.6}$$

$$- K_3R_g\theta_2 + C_3R_p\dot{\theta}_1 + K_3R_p\theta_1 = 0$$

$$I_1\ddot{\theta}_1 + R_p^{\,2}C_3\dot{\theta}_1 + R_p^{\,2}K_3\theta_1 - R_pR_gC_3\dot{\theta}_2 - R_pR_gK_3\theta_2 + R_pC_3\dot{X}_2 + R_pK_3X_2 = T_1 \tag{3.7}$$

$$I_2\ddot{\theta}_2 + R_g^{\,2}C_3\dot{\theta}_2 + R_g^{\,2}K_3\theta_2 - R_gR_pC_3\dot{\theta}_1 - R_gR_pK_3\theta_1 - R_gC_3\dot{X}_2 - R_gK_3X_2 = T_2 \tag{3.8}$$

The model was written into state space format and implemented in MATLAB for simulation with the ode45 differential equation solver.

3.2.2 Application of intrinsic cycle re-sampling method

In the following, signal analysis is now done to explore two questions:

a) How does the ICR result relate to order analysis in the simulation model?
b) How does ICR perform as an alternative condition monitoring tool?

a. Choosing an appropriate IMF

Before the above questions can be addressed, the first step is to choose an appropriate IMF for the analysis. To do this the relationship between the original gear casing velocity signal $\dot{X}_1$ and its IMFs is first considered. For this purpose the gear response was simulated over a 5 s period. The last 1 s of this response, after steady conditions have been reached, is now considered in the following analysis. In this steady state the variation of the rotational speed of the gear still remains due to the fluctuating load. For illustrative purposes, a section of 0.25 s of this signal is depicted in Figure 3.14(a). The low frequency fluctuation at 25 Hz, due to the variation in input torque, can easily be observed in this figure. Higher frequencies are the result of gear meshing which corresponds to 250 Hz (the 10^{th} order) at the nominal rotational speed of 1500 rpm. The response at this frequency and its harmonics is of great importance for obtaining information about the deterioration of the gear (i.e. stiffness). Basic Fourier analysis is performed in Figure 3.14(b). Except for the rotational frequency peak at 25 Hz and the gear mesh frequency of 250 Hz, it shows several sidebands around the gear mesh frequency. This is due to the fluctuation of the rotational speed caused by the fluctuating load.

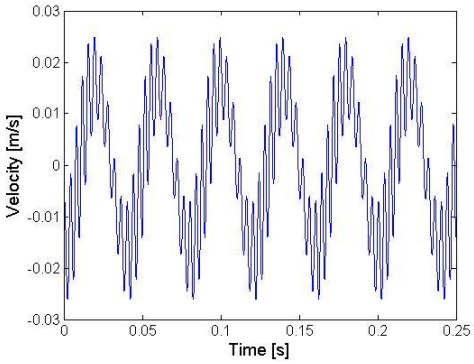

a. Velocity $\dot{X}_1$

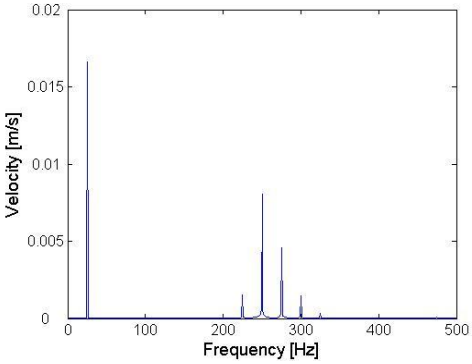

b. Fourier spectrum of velocity $\dot{X}_1$

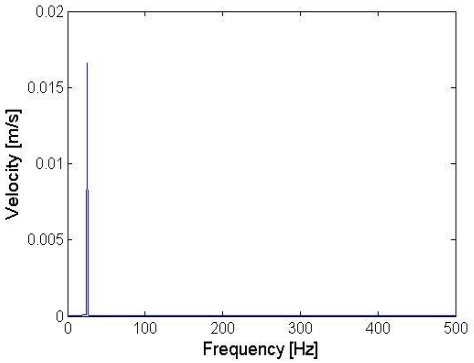

c. Fourier spectrum of 2nd IMF

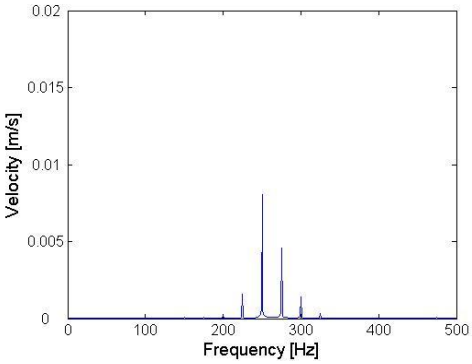

d. Fourier spectrum of 1st IMF

Figure 3.14 Velocity $\dot{X}_1$ and associated Fourier spectrum

EMD is now applied to the signal and the spectra of the 1st and 2nd IMFs are plotted in Figures 3.14(d) and (c) respectively. The 1st and 2nd IMFs successfully separate the lower and higher frequency content. This can of course also be achieved by using low and high pass filters but, in this case is accomplished empirically. The 2nd IMF captures the rotational frequency at 25 Hz while the 1st IMF extracts the gear mesh frequency content and its sidebands. Clearly, the 1st IMF which relates to the gear mesh frequency content, captures the changes of gear stiffness and is therefore the appropriate IMF for further analysis of the ICR method in condition monitoring.

b. Comparison of ICR result to order analysis in the simulation model

To investigate how the ICR results relate to order tracking analysis in this model, results from conventional order tracking analysis and ICR on the 1st IMF, are compared in Figure 3.15. Since the 1st IMF is focused on the gear mesh vibrations, the conventional order tracking analysis also focuses on gear mesh vibration for comparative purposes. The 10th order is extracted from the raw signal by Vold-Kalman filter order tracking (VKF-OT), through which the gear mesh order (10th order) is obtained. (A 20% relative filter bandwidth is used.). Then computed order tracking is applied to the extracted gear mesh order into order spectrum. For further comparison to the ICR results, the figure is normalized in terms of the highest order peak which renders Figure 3.15(a). The ICR method is applied to the 1st IMF and gives Figure 3.15(b) which is also normalized in terms of highest frequency peak.

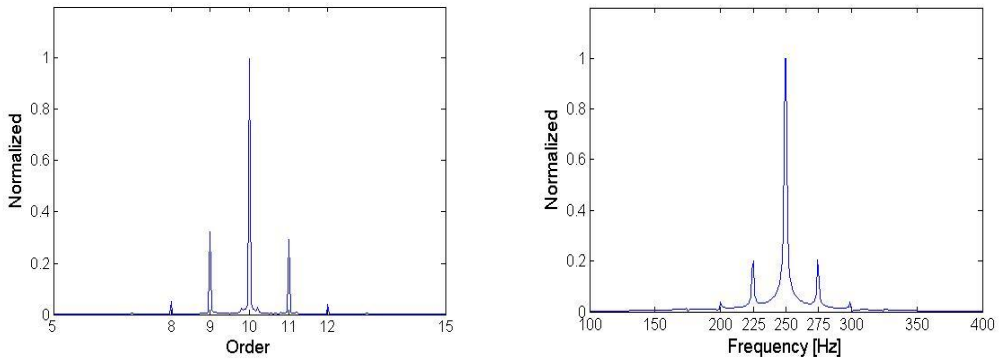

a. 10th order analysis b. ICR on 1st IMF

Figure 3.15 Comparison of COT and ICR results

Through comparison of Figures 3.15(a) and (b), it is firstly clear from the abscissa that unlike order tracking analysis in Figure 3.15(a), the ICR result remains in the frequency domain, in stead of the order domain, as is shown in Figure 3.15(b).

This is accomplished by employing the new sampling frequency of equation (2.12) in chapter 2, paragraph 2.3.2.

Secondly, from the two normalized figures it can be seen that both the order tracking and ICR spectral maps feature similar shapes with one main peak and evenly distributed sidebands. For the order map in Figure 3.15(a), the order sideband spacing is 1 with the 8^{th}, 9^{th}, 11^{th} and 12^{th} orders present. Similarly, the frequency sideband spacing in Figure 3.15(b) is 25 Hz with peaks at 200 Hz, 225 Hz, 275 Hz and 300 Hz. The 25 Hz corresponds to the nominal rotational speed. However, the ratio of the highest sideband to the main peak between two figures is slightly different. For Figure 3.15(a) this ratio is 0.3 and 0.2 for Figure 3.15(b). The difference is due to the decomposition of the 2^{nd} IMF as is shown in Figure 3.14(c). The 25 Hz amplitude modulation is the same frequency as the nominal rotational speed, which has been partly separated into the 2^{nd} IMF. This reflects the fact that the ICR method is influenced by the decomposition process of EMD. However, both figures share similar attributes in analyzing the order of interest.

Thirdly, the peaks on the order analysis results in Figure 3.15(a) are sharper than the ICR result in Figure 3.15(b). This also suggests a difference between the two methods. Firstly, the original sampling frequency in the simulation was set at $f_s = 8192\,Hz$ in Table 3.3. After re-sampling, the new sampling frequency for the ICR analysis changes to $f_{new} = \frac{S_{resample}}{t_{period}} = \frac{48001}{1} = 48001 Hz$ as defined in equation (2.12). (In this case, within a 1 s signal, there are 24 revolutions and 250 intrinsic cycles. The re-sampling interval in one revolution is $I = 2000$ (see Table 3.3). Thus the number of re-sampled intervals for the computed order tracking analysis is $24 \times 2000 = 48000$. To keep the same number of analysis samples for ICR, 192 intervals within one intrinsic cycle is chosen, therefore, the $f_{new} = 48001 Hz$). And the Nyquist frequency for this ICR analysis

is $f_{Nyquist} = \frac{f_{new}}{2} = 24000.5Hz$. For order analysis, the order sampling frequency is $O_{sample} = \frac{1}{2\pi/I} = \frac{1000}{\pi} = 318.3$ order and the Nyquist order is $O_{Nyquist} = \frac{O_{sample}}{2} = \frac{500}{\pi} = 159.15$ order. Considering the ratio of the dominant components in the order spectrum and the ICR results to their Nyquist values, a difference can therefore be calculated that the dominant nominal gear mesh vibrations, f_N, in the ICR spectrum occurs at $\frac{f_N}{f_{Nyquist}} = \frac{250}{24000.5}100\% = 1.04\%$ of $f_{Nyquist}$. However for order analysis, the corresponding gear mesh at the 10^{th} order, occurs at $\frac{O_{10th}}{O_{Nyquist}} = \frac{10}{159.1}100\% = 6.29\% \text{ of } O_{Nyquist}$. Clearly, the ratio of the frequency components in the ICR spectrum and the order component in order spectrum are different from their Nyquist values. As a result, the order spectrum in Figure 3.15(a) looks sharper than ICR spectrum in Figure 3.15(b). This indicates that the new sampling frequency for ICR analysis may influence the visual appearance of the of the spectrum map.

Lastly, it should always be borne in mind that ICR is strictly speaking not an order tracking analysis. It reflects changes of the signal itself. Only when the frequency variation in signals is caused by rotational speed, it may serve as an alternative order tracking approximation. Fortunately, in many practical applications for rotating machine vibrations, such an assumption is applicable. This is the case in this simulation study for a gearbox in good condition.

c. ICR as an alternative condition monitoring tool

Traditional signal processing methods

Subsequently a typical seeded fault is introduced. The gear mesh stiffness K_3 is reduced to 98% of the nominal gear mesh stiffness at an angle from $160°$ to $165°$ of the shaft rotation. Firstly, traditional signal processing methods are applied to the signals from the gearbox in good condition and with the seeded fault, so that a clear picture of how traditional signal processing methods respond to the fault can be obtained. Thus, time, frequency and order domain analyses are first compared in Figure 3.16.

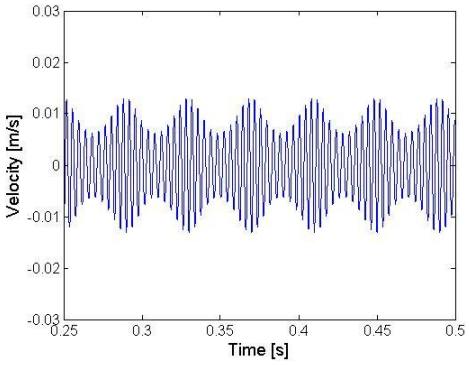

a. 1st IMF for good condition

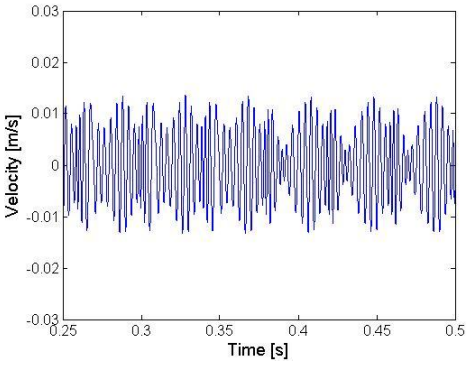

b. 1st IMF for fault condition

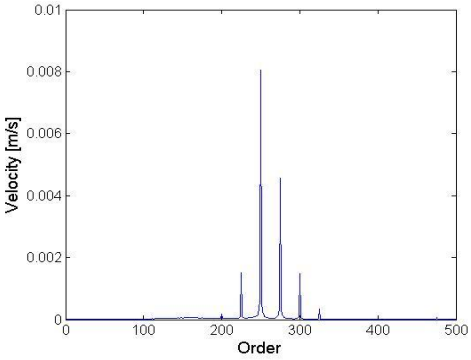

c. FFT on 1st IMF for good condition

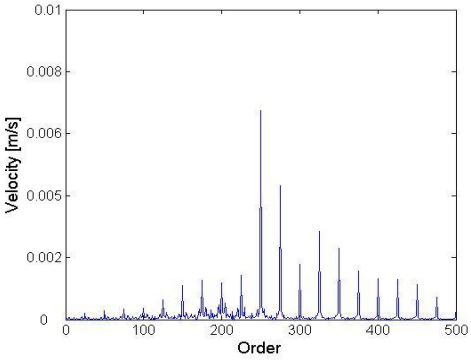

d. FFT on 1st IMF for fault condition

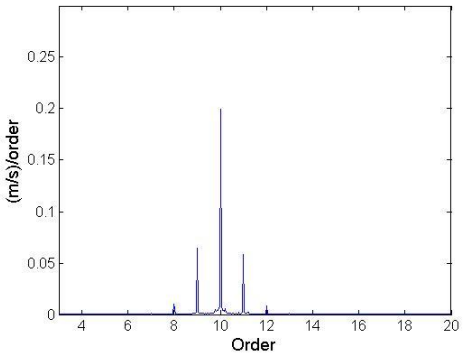

e. Order tracking for good condition

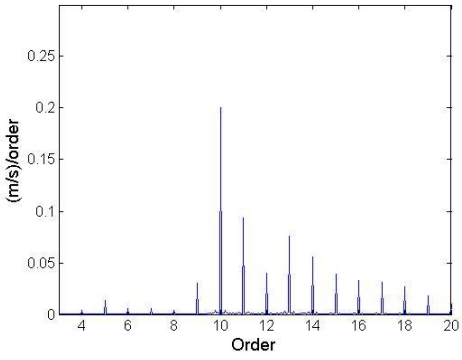

f. Order tracking for fault condition

Figure 3.16 Comparison of good and seeded fault conditions

The 1st IMF time domain velocity signals for good and fault conditions in Figures 3.16(a) and (b) show that the high frequency gear mesh signal has been extracted

from the original velocity. In Figures 3.16(a) and (b), the amplitude variations are both clearly visible. Comparing the two figures indicate that the gear mesh vibrations change due to the introduction of the fault.

In the frequency domain, Figures 3.16(c) and (d) show the frequency spectra of the 1st IMF signals. Sideband peaks are very clear in both figures. With the introduction of the fault, the corresponding spectrum in Figure 3.16(d) shows more sidebands and some of its peak amplitudes change. Figures 3.16(e) and (f) consider the order domain, to test the ability of the computed order tracking method for raw signals. Compared with Figure 3.16(d) in the frequency domain, the order domain spectrum features cleaner order components. This is due to the exclusion of speed variation effects. However by the reduction of gear mesh stiffness to 98%, more sidebands and order peak amplitude variations occur. This implies that the order tracking method also detects the changes in the system. In short, it may be noticed that traditional signal processing techniques detect the system changes in terms of amplitude changes in the time domain and peak amplitude changes in the spectrum as well as more sidebands appearance.

ICR as an alternative tool

Unlike the traditional methods discussed above, the way in which ICR responds to the fault, follows the fundamental characteristics of re-sampled IMF as is discussed in chapter 2 paragraph 2.3.2. The two aspects of the ICR results that respond to the fault are examined, namely the sidebands variation (S.V.) due to $A_{ICR}(t)$ and the value of the main frequency (M.F.) due to f_{ICR}. To trend the changes in the ICR results, a range of six fault conditions are considered. They are 100%, 99.6%, 99.2%, 99%, 98.5% and 98% of the original gear mesh stiffness. The ICR results for these cases are plotted in Figure 3.17.

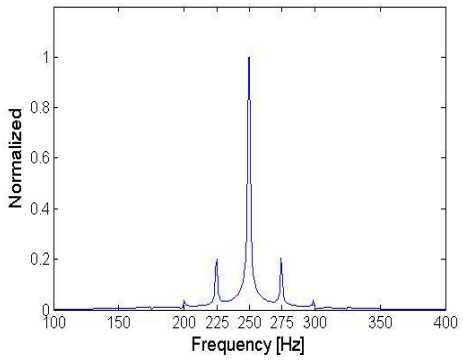

a.100% stiffness (good condition)
S.V.: two clear sidebands and peak ratio 0.2 ; M.F.: 250 Hz

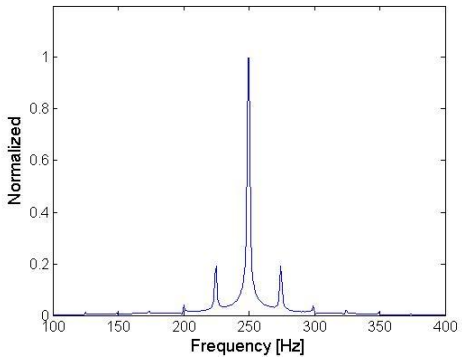

b. 99.6% stiffness
S.V.: two clear sidebands and peak ratio 0.19; M.F.: 250 Hz

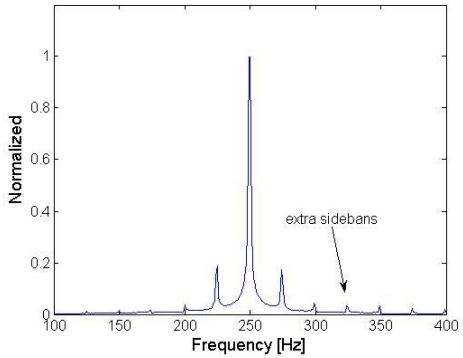

c. 99.2% stiffness;
S.V.: extra sidebands and peak ratio 0.185; M.F.:250 Hz

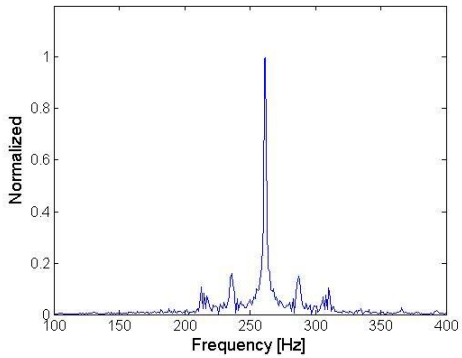

d. 99% stiffness
S.V.: 4 deformed extra sidebands M.F.:262 Hz

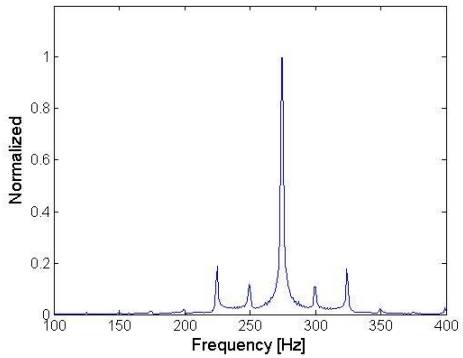

e. 98.5% stiffness
S.V.: 4 clear uneven amplitude sidebands M.F.: 275 Hz

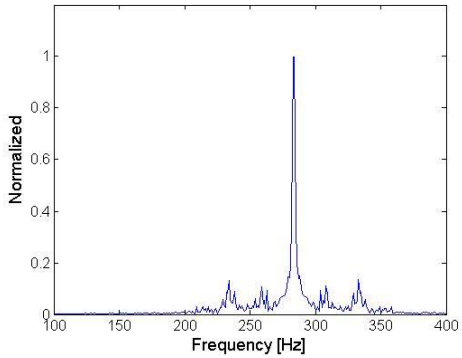

f. 98% stiffness
S.V.: more deformed sidebands M.F.: 283 Hz

Figure 3.17 ICR results on different fault conditions

Figure 3.17 shows the variation of the ICR results with the development of the fault. Instead of many sidebands appearing as happens in the frequency and order domains, the two aspects (S.V. and M.F.) show the progress of the fault. For this simulation study, the faults can be categorized into two stages in terms of M.F: Initially (Figures 3.17(a) to (c)) the M.F. is stationary. For Figures 3.17(d) to (f) M.F. is varying. This corresponds to point (a) in the guidance provided chapter 2 in paragraph 2.3.2.

In the first stage, the peak ratio between the highest sidebands to the main frequency peak can be used as a distinct indicator of changes in the signals. The S.V. ratio decreases with the development of the fault from 0.2 to 0.19 and then change to 0.185. This indicates that a variation of $A_{ICR}(t)$ occurs, albeit very small. Considering further the S.V. effects, it can be seen that (especially in Figure 3.17(c)) extra sidebands grow with the development of the fault. This further confirms that $A_{ICR}(t)$ is varying and it requires more sidebands to represent these changes. Due to the stationarity of the M.F. as well as the above discussions on the changes in S.V., it may be concluded that during the first stage, the fault does not severely influence the 1st IMF or gear mesh vibrations, although it is developing.

In the second stage, the M.F. values may be used as a distinct indicator of the system changes. With the development of the fault, the M.F. becomes 262 Hz, 275 Hz and 283 Hz respectively. It is also found that the sidebands become uneven in amplitude in Figures 3.17(d), (e) and (f). The shapes of the sidebands become severely deformed in Figures (d) and (f). However, it should be noted that in figure (e) sidebands are smoother than the other two figures. Especially it is smoother than figure (d) where the fault on gear mesh stiffness is smaller. In

such a case, according to the discussion of chapter 2 paragraph 2.3.2, M.F. values should be first considered as the indicator of fault severity, despite with smoother sidebands, figure (e) however shows more serious fault than figure (d) due to the bigger value of M.F. Besides, the smoother sidebands of figure (e) indicate that, compared to the other two fault conditions in (d) and (f), the amplitude part of the re-sampled IMF, $A_{ICR}(t)$, can be represented by much simpler sidebands in (e). In fact, it is an intermediate period of fault development. In such a case, when M.F. is different, the S.V. is not a decisive factor to determine the severity of the fault however M.F. should be considered first. According to the theoretical studies in chapter 2 paragraph 2.3.2 guidance (c), in this second stage, the seeded faults severely influence the 1st IMF or gear mesh vibrations, the shift of M.F. with severe S.V. indicates a big variation of signals, thus apparently the severity of the damage is increasing.

Comparisons of ICR to tradition signal processing methods

In the end, one should compare the differences between the ICR with traditional condition monitoring methods. The good and fault condition (at 98% nominal gear mesh stiffness) figures are plotted for comparison. All figures are normalized in terms of highest spectrum peaks in Figure 3.18.

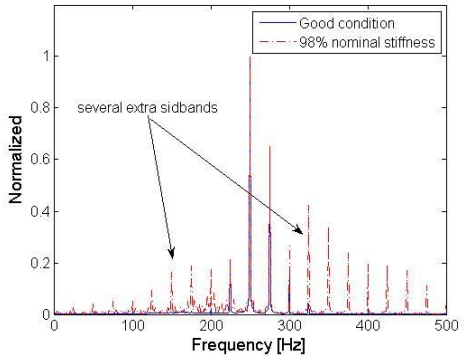

a. Frequency domain on 1st IMF

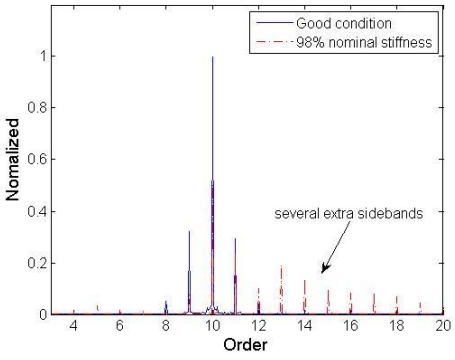

b. Order domain

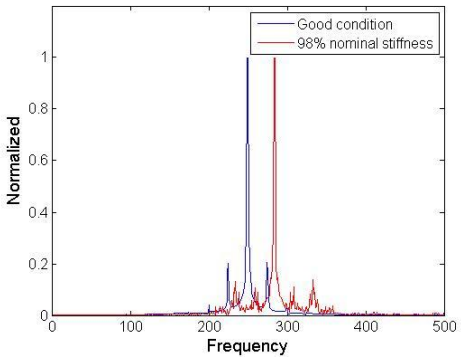

c. ICR result

Figure 3.18 Comparisons between traditional methods with ICR result

Figure 3.18 clearly shows that the traditional methods in figures (a) and (b) indicate the fault is mainly revealed in terms of several extra sidebands as are indicated in both figures. There is significant variation in the frequencies and order peaks. To trend the system changes, one needs to attend to all these peaks. However, instead of presenting several extra sidebands, the ICR technique in

figure (c) with its fundamental characteristics of re-sampled IMF, S.V. and M.F., can be used to trend the changes of system variations. It may be observed that the ICR method also present distinct changes in the results, especially for the unique shift of the M.F., where traditional methods do not have similar indicators. This suggests the ICR technique as an alternative method for machine fault diagnostic with distinct indicators for condition monitoring purposes.

3.3 Summary

In this chapter, two simulation models are used to explore the abilities of three novel improved order tracking techniques. The first simple rotor model is used to demonstrate the ability of VKC-OT and IVK-OT. Under non-stationary and noisy signal environments, the VKC-OT technique presents its unique ability to feature clear and focused order component. This overcomes the disadvantages of non-stationarity in the Vold-Kalman filter result and the inability of separating orders using computed order tracking. The VKC-OT no doubt provides a better perspective to inspect individual order components.

IVK-OT combines the empirical nature of IMF and the strict mathematical nature of VKF-OT to explore a sequential way of using two methods to separate modulated order signals which provides an edge for order tracking techniques to obtain vibrations that modulate orders, especially for those vibrations that are not synchronous with rotational speed.

Finally, the gear mesh model proves the ability of ICR technique. The re-sampling process takes advantage of an intrinsic mode function of symmetric, oscillating and zero mean nature to reconstruct an intrinsic mode function into a re-sampled intrinsic mode function which suppress frequency variations of the signal. In this way an approximation of order tracking effects is obtained without the need for rotational speed. At the same time, the method further brings

advantages for condition monitoring, in that the re-sampled intrinsic mode function offers more specific characteristics for trending machine conditions. These simulation studies lay a good foundation for the experimental analysis in the following chapter.